

See discussions, stats, and author profiles for this publication at: <https://www.researchgate.net/publication/261739480>

# Oxygen-Vacancy-Induced Polar Behavior in (LaFeO<sub>3</sub>)<sub>(2)</sub>/(SrFeO<sub>3</sub>) Superlattices

ARTICLE *in* NANO LETTERS · APRIL 2014

Impact Factor: 13.59 · DOI: 10.1021/nl500601d · Source: PubMed

---

CITATIONS

4

READS

150

## 10 AUTHORS, INCLUDING:



Rohan Mishra

Washington University in St. Louis

27 PUBLICATIONS 152 CITATIONS

[SEE PROFILE](#)



Juan Salafranca

Complutense University and Oak Ridge Nation...

35 PUBLICATIONS 229 CITATIONS

[SEE PROFILE](#)



Albina Y Borisevich

Oak Ridge National Laboratory

186 PUBLICATIONS 2,632 CITATIONS

[SEE PROFILE](#)

# Oxygen-Vacancy-Induced Polar Behavior in $(\text{LaFeO}_3)_2/(\text{SrFeO}_3)$ Superlattices

Rohan Mishra,<sup>\*,†,‡,§,▽</sup> Young-Min Kim,<sup>‡,§,▽</sup> Juan Salafranca,<sup>‡,□</sup> Seong Keun Kim,<sup>||,⊥</sup> Seo Hyoung Chang,<sup>||</sup> Anand Bhattacharya,<sup>||,△</sup> Dillon D. Fong,<sup>||</sup> Stephen J. Pennycook,<sup>#</sup> Sokrates T. Pantelides,<sup>†,‡</sup> and Albina Y. Borisevich<sup>\*,‡</sup>

<sup>†</sup>Department of Physics and Astronomy, Vanderbilt University, Nashville, Tennessee 37235, United States

<sup>‡</sup>Materials Science and Technology Division, Oak Ridge National Laboratory, Oak Ridge, Tennessee 37831, United States

<sup>§</sup>Division of Electron Microscopic Research, Korea Basic Science Institute, Daejeon 305-806, Republic of Korea

<sup>||</sup>Materials Science Division and <sup>△</sup>Nano Science and Technology Division, Argonne National Laboratory, Argonne, Illinois 60439, United States

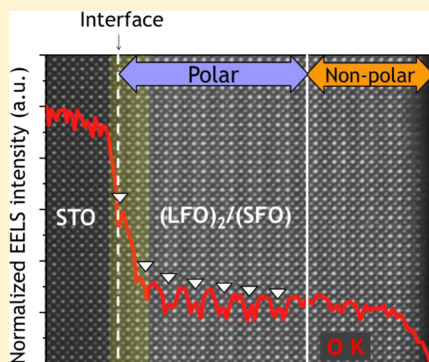
<sup>⊥</sup>Electronic Materials Research Center, Korea Institute of Science and Technology, Seoul 136-791, Republic of Korea

<sup>#</sup>Department of Materials Science and Engineering, University of Tennessee, Knoxville, Tennessee 37996, United States

<sup>□</sup>Grupo de Física de Materiales Complejos, Universidad Complutense, 28040 Madrid, Spain

## Supporting Information

**ABSTRACT:** Complex oxides displaying ferroelectric and/or multiferroic behavior are of high fundamental and applied interest. In this work, we show that it is possible to achieve polar order in a superlattice made up of two nonpolar oxides by means of oxygen vacancy ordering. Using scanning transmission electron microscopy imaging, we show the polar displacement of magnetic Fe ions in a superlattice of  $(\text{LaFeO}_3)_2/(\text{SrFeO}_3)$  grown on a  $\text{SrTiO}_3$  substrate. Using density functional theory calculations, we systematically study the effect of epitaxial strain, octahedral rotations, and surface terminations in the superlattice and find them to have a negligible effect on the antipolar displacements of the Fe ions lying in between  $\text{SrO}$  and  $\text{LaO}$  layers of the superlattice (i.e., within  $\text{La}_{0.5}\text{Sr}_{0.5}\text{FeO}_3$  unit cells). The introduction of oxygen vacancies, on the other hand, triggers a polar displacement of the Fe ions. We confirm this important result using electron energy loss spectroscopy, which shows partial oxygen vacancy ordering in the region where polar displacements are observed and an absence of vacancy ordering outside of that area.



**KEYWORDS:** Transition-metal oxides, multiferroics, polar oxides, DFT calculations, scanning transmission electron microscopy, oxygen vacancies

Multiferroics display simultaneous magnetic and ferroelectric ordering and thereby offer the prospect of controlling magnetism with an electric field or vice versa. Therefore, they hold promise for new technologies and improved devices for data storage and manipulation, magnetic-field sensing, and other applications. Multiferroics are rare,<sup>1</sup> however, because ferroelectricity generally requires a d<sup>0</sup> cation that undergoes off-centering,<sup>2</sup> while magnetism arises from partially filled d-orbitals. A decade of search has resulted in a handful of materials that overcome these conventions and display multiferroic behavior.<sup>3–9</sup> In such materials, which belong to the family of complex oxides, multiferroicity has been achieved predominantly by using two cations, one for each task. For instance, in  $\text{BiFeO}_3$ , the lone pair on  $\text{Bi}^{3+}$  drives the ferroelectric ordering, while the 3d electrons of  $\text{Fe}^{3+}$  provide the magnetic moment.<sup>3</sup> In  $\text{EuTiO}_3$ , the highly localized 4f electrons of  $\text{Eu}^{2+}$  provide the magnetic moment, while the 3d<sup>0</sup>  $\text{Ti}^{4+}$  cation undergoes polar distortion.<sup>4,5</sup>

Complex oxides, however, typically have finite concentrations of vacancies,<sup>10,11</sup> which together with the fine balance between the spin, charge, orbital, and lattice degrees-of-freedom, control many properties.<sup>12,13</sup> The question arises then whether it is possible to achieve multiferroic behavior by tuning the concentration and ordering of oxygen vacancies in an oxide. Such a strategy would open up an additional path for attaining multiferroic behavior, while leaving us the freedom to manipulate the cations. Recent studies have revealed the role of oxygen vacancies on the structural, magnetic, and electrical behavior of complex oxides.<sup>10,11,14–17</sup> Oxygen vacancies have also been reported to assist in the switching behavior of ferroelectric thin films by compensating for polarization induced interface or surface charges.<sup>11,18–20</sup> However, utilizing

**Received:** February 14, 2014

**Revised:** April 7, 2014

**Published:** April 15, 2014

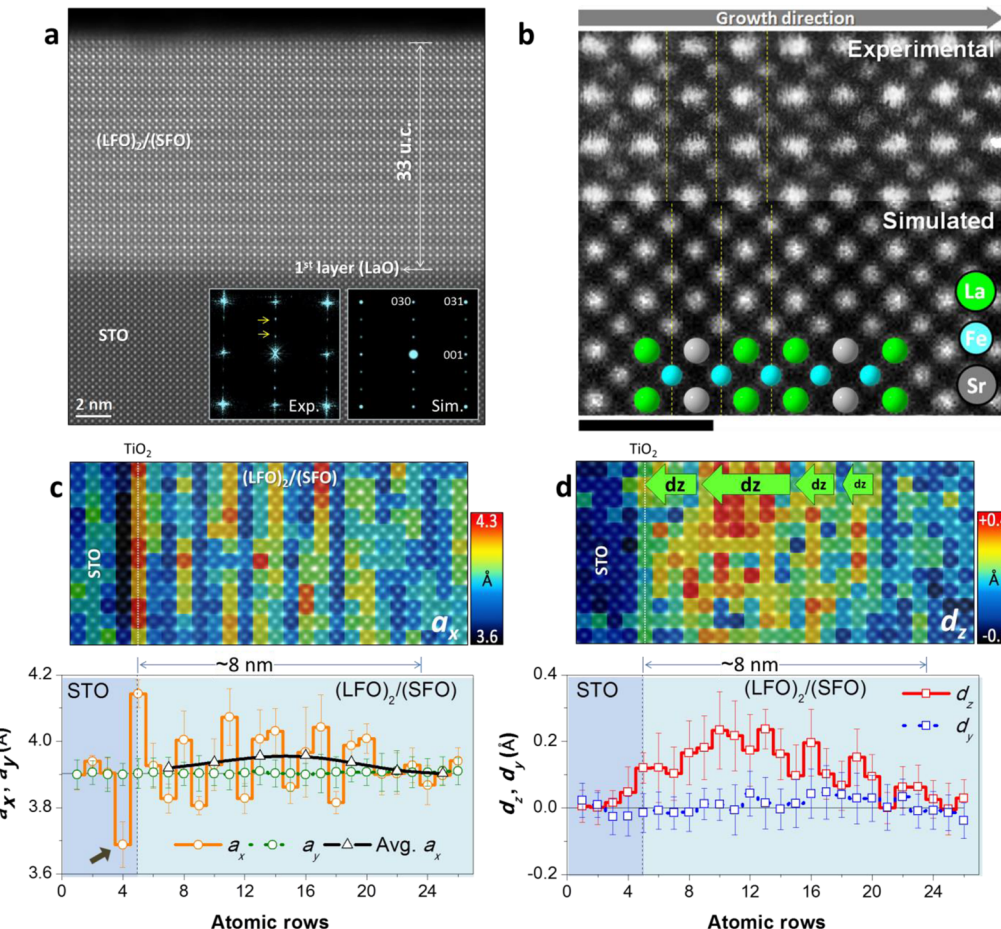


**Figure 1.** Superlattice structure and atom position quantifications for lattice distortion and polarization mappings. (a) ADF STEM image of  $[100]_{pc}$ -oriented  $(\text{LaFeO}_3)_2/(\text{SrFeO}_3)$  superlattice film grown on  $\text{TiO}_2$ -terminated (100)  $\text{SrTiO}_3$  substrate. The thickness of the film is measured to be 33 unit cells, and the interface between the film and the substrate appears atomically well-defined and coherent, free of lattice defects. The insets in the image show fast Fourier transform (FFT) of the image and a simulated electron diffraction pattern using the superlattice atomic model, respectively. Superlattice reflections to manifest the 2:1 periodicity of  $\text{LaFeO}_3$  and  $\text{SrFeO}_3$  are noticeable in the FFT (marked with arrows) and coincide with the simulation result. (b) High magnification ADF STEM image (upper panel) and simulated image (lower panel) of the superlattice structure. The atomic model of the superlattice used for the simulation is overlaid on the image. The scale bar is 1 nm. (c) Map of the out-of-plane lattice spacing ( $\text{A}-\text{A}$  interatomic distance in the  $\text{ABO}_3$  structure) and line profiles of both out-of-plane ( $a_x$ , solid orange) and in-plane ( $a_y$ , dotted green) directions. Avg.  $a_x$  (solid black) shows the out-of-plane expansion within individual  $(\text{LaFeO}_3)_2/(\text{SrFeO}_3)$  units. (d) Fe cation displacement map obtained along the out-of-plane ( $d_z$ , solid red) direction representing characteristic polarization behavior of the sample and the averaged line profiles of the displacements with respect to the out-of-plane ( $d_z$ , solid red) and in-plane ( $d_y$ , dotted blue) directions. The error bars show the standard deviations of the averaged measurements for each vertical atomic layer in the maps.

oxygen vacancies as a driving force for achieving polar order in nonpolar materials has not been explored.

In this work, we demonstrate oxygen vacancy driven polar behavior in  $(\text{LaFeO}_3)_2/(\text{SrFeO}_3)$  superlattices, using a combination of scanning transmission electron microscopy (STEM), core-loss electron energy loss spectroscopy (EELS), and density functional theory (DFT) based calculations. We show polar displacement of magnetic Fe ions in a superlattice of  $(\text{LaFeO}_3)_2/(\text{SrFeO}_3)$  grown along the  $[001]$  direction on a  $\text{SrTiO}_3$  substrate using STEM imaging. Using DFT calculations, we systematically study the effect of epitaxial strain, octahedral rotations, and surface terminations in the superlattice and find them to have a negligible effect on the antipolar displacements of the Fe ions lying in between  $\text{SrO}$  and  $\text{LaO}$  layers of the superlattice (i.e., within  $\text{La}_{0.5}\text{Sr}_{0.5}\text{FeO}_3$  unit cells). The introduction of oxygen vacancies, on the other hand, triggers a polar displacement of the Fe ions. We confirm this important result using EELS, which shows partial ordering of

oxygen vacancies into layers parallel to the interface, with periodicity matching the cation superlattice in the region where polar displacements are observed, and does not show any ordering outside of that area.

We have chosen a 12.4 nm (corresponding to 33 unit cells) thick superlattice with two unit cells of  $\text{LaFeO}_3$  followed by one unit cell of  $\text{SrFeO}_3$ , grown epitaxially on a  $[001]$   $\text{SrTiO}_3$  substrate, as our model system. Bulk  $\text{LaFeO}_3$  exists in the orthorhombic  $Pbnm$  space group with  $a^-a^-c^+$  octahedral tilt pattern<sup>21,22</sup> and is a G-type antiferromagnetic insulator with a high Néel temperature of 750 K.<sup>23</sup> Bulk  $\text{SrFeO}_3$ , on the other hand, is an antiferromagnetic metal with cubic  $Pm\bar{3}m$  space group symmetry ( $a^0a^0a^0$  tilt) and is prone to the formation of oxygen vacancies, due to the high formal valence of +4 on iron.<sup>24</sup> The antiferromagnetism itself arises from a helical ferromagnetic spin structure.<sup>24</sup> The oxygen defect chemistry in the bulk solid solution of  $\text{La}_{1-x}\text{Sr}_x\text{FeO}_{3-\delta}$  has been well-studied due to its superior ionic and electronic conductivity and

catalytic performance.<sup>25–32</sup> In particular, compounds with a general stoichiometry of  $\text{LaSr}_2\text{Fe}_3\text{O}_{9-\delta}$  are known to form oxygen-deficient phases such as  $\text{LaSr}_2\text{Fe}_3\text{O}_8$  and  $\text{LaSr}_2\text{Fe}_3\text{O}_{8.417}$ , wherein the oxygen vacancies selectively order into every third  $\text{FeO}_2$  layer, along a particular crystallographic axis, to give rise to four- or five-coordinate polyhedra, followed by two layers of  $\text{FeO}_2$  octahedra, and are commonly known as brownmillerite polymorphs.<sup>31,32</sup> It should be noted that, in such compounds, the La and Sr cations are distributed randomly. On the other hand, compounds with a stoichiometry of  $\text{La}_2\text{SrFe}_3\text{O}_{9-\delta}$ , which is similar to the superlattice in this study, have a large concentration of oxygen vacancies that are distributed randomly.<sup>25–29</sup>

The typical superlattice thin-film structure of  $(\text{LaFeO}_3)_2/\text{(SrFeO}_3)$  oriented along  $[100]_{\text{pc}}$  (subscript pc denotes pseudocubic) direction is shown in an annular dark field (ADF) STEM image (Figure 1a), where the contrast is approximately proportional to  $Z^2$ , with Z being the atomic number.<sup>33</sup> Thus, in this imaging mode, the brightest features are La columns ( $Z = 57$ ), while the oxygen ( $Z = 8$ ) columns remain largely invisible due to dynamic range constraints. From the image, we see that the interface between the superlattice film and the substrate is clearly defined and coherent without lattice defects. The film itself shows clear contrast modulation with a three-unit cell periodicity consistent with the repetition of  $(\text{LaO})_2/(\text{SrO})$  layers with  $\text{FeO}_2$  layers in between. A diffractogram of the image generated via fast Fourier transform (FFT) shows superlattice reflections corresponding to the tripled periodicity of the superlattice and is in excellent agreement with the simulated pattern (see insets in Figure 1a). However, a very close examination of the image at higher magnification (upper panel in Figure 1b) shows that the Fe atoms are displaced toward one of the AO layers (where A = Sr, La) in the direction of the substrate. This intriguing polar behavior is brought out more clearly by comparison to the simulated image (lower panel in Figure 1b), where the Fe columns are situated exactly between the neighboring AO layers.

To characterize the polar displacements and the lattice distortions in the superlattice sample as a function of distance from the interface,<sup>10,34–36</sup> we quantify the A-site and B-site atomic positions from the ADF STEM image and calculate structural parameters in the out-of-plane and in-plane directions as shown in the schematic in the Supporting Information (Figure S1). The top panels in Figure 1c and d show the 2D color maps of out-of-plane A-site interatomic distance ( $a_x$ ) and Fe cation displacement ( $d_z$ ), respectively, overlaid with the corresponding ADF image. The profiles for both in-plane and out-of-plane directions computed by averaging over the vertical columns of the respective maps are given in the bottom panels. Note that the in-plane lattice spacing ( $a_y$ ) shows no significant changes as expected owing to epitaxial constraints.

From the out-of-plane A-site lattice spacing map (Figure 1c), we see periodic expansion and contraction of the AO–AO layers. The distortions begin with a substantial contraction of the outermost (SrO–SrO) layer of the  $\text{SrTiO}_3$  substrate (see the arrow in the line profile) followed by a large expansion of the first SrO–LaO layer between the substrate and the film. More details about the observed contraction of the outermost (SrO–SrO) layer are presented in the Supporting Information. This is followed by an expansion of the LaO–LaO layers and contraction of the LaO–SrO layers that persists deeper into the film, with the triple periodicity templated by the superlattice.

However, the magnitude of the lattice spacing oscillations is gradually damped and eventually goes close to zero net at  $\sim 8$  nm away from the interface. This behavior cannot be explained by the difference in ionic radii of La and Sr, since in that case LaO–LaO spacing would have been the shortest, and LaO–SrO the longest ( $r_{\text{La}^{3+}} = 1.3 \text{ \AA}$ ,  $r_{\text{Sr}^{2+}} = 1.4 \text{ \AA}$ ); therefore other phenomena must be in play.<sup>37</sup> In particular, the molar volume of  $(\text{La}_{1-x}\text{Sr}_x)\text{FeO}_{3-\delta}$  solid solutions in the bulk has been shown to increase monotonically, albeit in a nonlinear manner, with increasing oxygen vacancy content, a behavior common for many ionic oxides and referred to as chemical expansivity.<sup>28,38,39</sup> For an epitaxially constrained film, oxygen vacancies lead to an increase in the out-of-plane lattice spacing. Recent studies show that this chemical expansivity holds down to the atomic scale.<sup>10</sup> Besides, the expansion of the LaO–LaO layers followed by the contraction of the LaO–SrO layers is also reminiscent of the brownmillerite polymorphs in bulk  $\text{LaSr}_2\text{Fe}_3\text{O}_{9-\delta}$  perovskites, where the oxygen deficient layers with 4-fold or 5-fold coordination of Fe atoms expand while the octahedral layers contract.<sup>31,32</sup> Starting from the first SrO layer in the film, we take the sum of the two SrO–LaO layer contractions and the succeeding LaO–LaO layer expansion to estimate the overall expansion within every  $(\text{LaFeO}_3)_2/\text{(SrFeO}_3)$  unit. This average expansion (avg.  $a_x$ ) profile as shown in Figure 1c indicates a gradual change in the concentration of oxygen vacancies, which increases from the interface and reaches a maximum at around  $\sim 4$  nm inside the film, after which it decreases gradually.<sup>40</sup> We checked for the repeatability of the observed patterns of variations of lattice spacings and polar displacements and found them to be present at different regions of the film, from the very first scan, and stable with respect to beam irradiation within experimental timeframes (see details in Supporting Figure S2), which suggests that the oxygen vacancies were induced during the growth stage as opposed to being induced by the electron beam.<sup>41</sup>

The map of the out-of-plane Fe cation displacements (Figure 1d) shows clear evidence of polar behavior in the superlattice near the interface. Such polar displacements are striking given the fact that neither  $\text{SrFeO}_3$  nor  $\text{LaFeO}_3$  are polar in their bulk form. We find that the Fe atoms are displaced toward the interface and the magnitude of their displacement ( $d_z$ ) reaches a maximum of  $\sim 0.23 \text{ \AA}$  around 2–3 nm away from the interface and then gradually decreases to zero  $\sim 8$  nm into the film. A comparison with the lattice spacing maps in Figure 1c and especially with the average lattice expansion (Avg.  $a_x$ ) shows a near-perfect overlap between the regions of the superlattice showing polar behavior and AO–AO lattice modulation. Besides the long-range behavior of polarization, we also observe modulations matching the superlattice periodicity, where the Fe displacement increases within the  $\text{LaFeO}_3$  unit cell and decreases in the two following  $\text{La}_{0.5}\text{Sr}_{0.5}\text{FeO}_3$  unit cells. While certain inhomogeneity in both lattice expansion and Fe cation displacements is observed across the image, both the long-range behavior and the short-range oscillations related to superstructure periodicity are clearly visible.

The overall shape of polarization is typical of a polar layer in contact with a metal electrode, where the polarization is suppressed at the interface and can be described by the Kretschmer-Binder model.<sup>42,43</sup> In our superlattice, we have a metallic phase of  $\text{La}_{1-x}\text{Sr}_x\text{TiO}_3$  owing to the observed cationic mixing of La and Sr within 1–2 monolayers into  $\text{SrTiO}_3$  as shown in the Supporting Figure S3.<sup>44</sup> Thus, the system we are

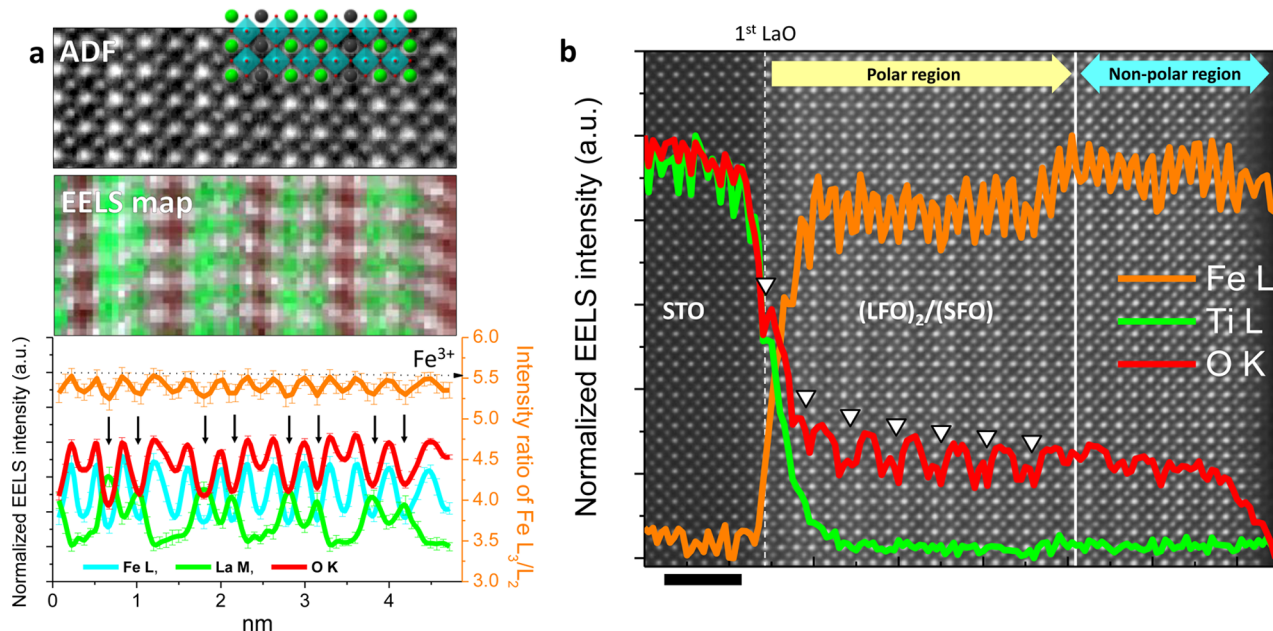


**Figure 2.** (a) ADF STEM image of the [100]<sub>pc</sub>-oriented  $(\text{LaFeO}_3)_2/(\text{SrFeO}_3)$  superlattice structure selected for core-loss EELS mapping (top panel figure) and the resulting EELS map (middle panel figure) to show the spatial distribution of Fe (cyan), La (green), and O (red) atoms. The line profiles of each element averaged over the vertical atomic rows appear in the bottom panel. The O vacancy containing planes contain arrows and coincide with the La planes. To see if the valence state of Fe changes through the structure, the EELS intensity ratio of the L<sub>3</sub> to L<sub>2</sub> peaks of the Fe L<sub>2,3</sub> edge is measured by the second derivative method, which is overlaid on the graph with the right side vertical axis (orange). (b) A representative core-loss EELS result of Fe L, Ti L, and O K edges measured across the whole thickness of the superlattice film on SrTiO<sub>3</sub>. The white dotted line indicates the position of the first LaO layer deposited on the outmost TiO<sub>2</sub> layer of the SrTiO<sub>3</sub> substrate. The solid white line divides the region with partial oxygen vacancy ordering in the LaFeO<sub>3</sub> layers from the upper part without the ordering. Scale bar, 2 nm.

looking at can be regarded as a polar/metallic heterostructure with spontaneous polarization directed toward the interface. We also observe that the polarization caused by interface phenomena persists for up to three unit cells into the SrTiO<sub>3</sub> substrate before disappearing. This induced polarization behavior is consistent with the theoretical description of the ionic relaxation occurring in the conductive metal oxide electrode to stabilize the ferroelectric phase by the “surface-capacitor” effect.<sup>42,45–47</sup> Maps of lattice spacings and displacements with a larger field of view are shown in Supporting Figure S4 and demonstrate again the direct correlation between the polar order and the lattice modulations.

In Figure 2a, we show an atomic resolution ADF STEM image along with an EELS map composed of Fe L (cyan), La M (green), and O K (red) edges, for the corresponding region. From the EELS map, we can visualize the periodic deficiency of oxygen in every LaO layer. The averaged line profiles for each element shown in the bottom of the figure more clearly present the characteristic dips of EELS intensities of O K edge observed at every LaO layer (marked with arrows). Evidence for oxygen vacancies in the LaFeO<sub>3</sub> layers also comes from the significant suppression of a prepeak in the O K edge fine structure as shown in the Supporting Information (Figure S5). These data unequivocally demonstrate that oxygen vacancies are concentrated within the repeating LaFeO<sub>3</sub> layers. It also confirms that the chemical expansion is responsible for the observed increase in lattice spacing at every LaO-LaO layer in the superlattice (Figure 1c). The intensity ratio of the L<sub>3</sub> to L<sub>2</sub> peaks of the Fe L<sub>2,3</sub> edge across the sample is overlaid on the bottom graph with a right vertical axis, which was measured by the second derivative method.<sup>48</sup> For the measured Fe L<sub>2,3</sub> ratio,<sup>49,50</sup> the valence of Fe can be estimated to be +3, which appears to be

constant throughout the film. The fine structures of Fe L<sub>2,3</sub> edges are presented in the Supporting Information (Figure S6). This invariant valence state of Fe ions in the superlattice in the presence of a large charge imbalance between different A cation layers can only be possible in the presence of a varying concentration of oxygen vacancies.

Even more striking evidence for the role of oxygen vacancy distribution in the polar behavior of the superlattice comes from the EELS line scan data obtained across the entire thickness of the superlattice (Figure 2b). From the normalized intensity profiles for Fe, O, and Ti, we find that Ti enters into 2–3 unit cells of the superlattice, while Fe barely diffuses into the SrTiO<sub>3</sub> substrate. The O-deficiency is clearly observed to be initiated at the first LaO layer and reoccurs periodically at the LaFeO<sub>3</sub> layers up to the solid line marked on the graph, at about 8 nm. After this line, the ordered vacancy arrangement breaks down, and so does the polar behavior of the superlattice, as well as the observed lattice modulation.

Although it is possible to attribute the overall shape of polarization to that of a typical metal/ferroelectric system, an intriguing question is what drives the polar displacements within a superlattice made up of two materials that are nonpolar in their bulk form. Multiple structural, chemical, and electronic factors could contribute to this behavior. Thus, to answer this question, we use DFT-based calculations, where we can examine individually the influence of each parameter such as epitaxial strain, octahedral rotations, surface termination, and oxygen vacancies on the displacement patterns of Fe atoms (and hence polar behavior) in  $(\text{LaFeO}_3)_2/(\text{SrFeO}_3)$  superlattices.

We begin by examining the displacement of Fe atoms in a  $(\text{LaFeO}_3)_2/(\text{SrFeO}_3)$  superlattice without any octahedral tilts

as shown in Figure 3a, which is epitaxially strained to theoretical  $\text{SrTiO}_3$  lattice parameters. We find the Fe (O)

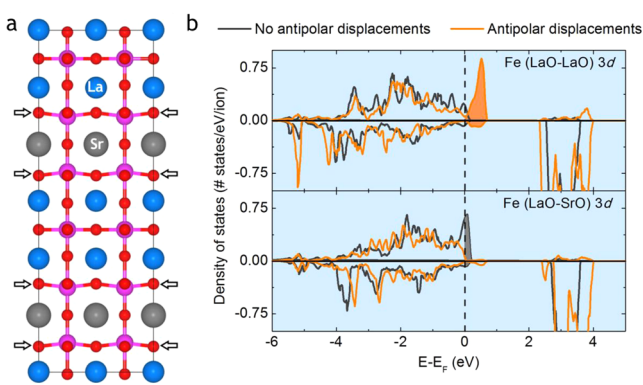


**Figure 3.** (a) A supercell of  $(\text{LaFeO}_3)_2/(\text{SrFeO}_3)$  without any octahedral tilts, showing the displacement of the Fe (pink color) and O ions (red color) lying in between LaO and SrO layers (marked with arrows). The Fe ions move toward the SrO layers, while the O ions move toward LaO layers. (b) Spin-resolved Fe 3d density of states, calculated using GGA+U, showing the transfer of holes (shaded) from Fe atoms lying between LaO-SrO layers to those lying between LaO-LaO layers on permitting the energy-lowering antipolar displacements.

atoms in the  $\text{La}_{0.5}\text{Sr}_{0.5}\text{FeO}_3$  units displace toward the SrO (LaO) layer from the centrosymmetric position, while the Fe (O) atoms in between two LaO layers (i.e., within the  $\text{LaFeO}_3$  unit cell) remain equidistant. The  $(\text{LaFeO}_3)_2/(\text{SrFeO}_3)$  superlattice periodicity in turn leads to an overall antipolar displacement pattern on looking at two neighboring  $\text{La}_{0.5}\text{Sr}_{0.5}\text{FeO}_3$  unit cells. We also find that the magnitude of these antipolar displacements is only  $0.05 \text{ \AA}$ , much smaller compared to the experimental displacements.<sup>51</sup>

The antipolar displacements appear to be governed by redistribution of electrons caused by different nominal valence of the two A-cations, with  $\text{O}^{2-}$  ions within the  $\text{La}_{0.5}\text{Sr}_{0.5}\text{FeO}_3$  unit cells displacing toward the nominally more positive  $\text{La}^{3+}$  ions due to Coulomb attraction, and the Fe ions with a nominal valence of +3.5 being repelled by  $\text{La}^{3+}$  ions toward  $\text{Sr}^{2+}$ . Similar distortions have been reported in bulk perovskites containing two cations with different oxidation states at the A-site and a d<sup>0</sup> cation at the B-site.<sup>52</sup> In such compounds, the d<sup>0</sup> cation undergoes an off-center distortion to facilitate layered ordering of the A-site cations lowering the electrostatic energy of the system.<sup>52</sup> Similarly, there are examples of bulk perovskites containing a non-d<sup>0</sup> cation such as Mn at the B-site, sandwiched between alternating layers of rare-earth ( $\text{R}^{3+}$ ) and alkaline-earth (A<sup>2+</sup>) cations, where the  $\text{MnO}_2$  layers buckle such that O ions are displaced toward R<sup>3+</sup> ions.<sup>53</sup> Off-center distortions of non-d<sup>0</sup> Mn ions have also been reported at the surface of  $\text{La}_{1-x}\text{Sr}_x\text{MnO}_3$  films and at the interface of  $\text{La}_{1-x}\text{Sr}_x\text{MnO}_3/\text{PbTiO}_3$  films in previous theoretical studies.<sup>54,55</sup> In the present study, the artificial ordering of the SrO and LaO layers achieved through molecular beam epitaxy drives the off-center distortion of the non-d<sup>0</sup> Fe ions.

The antipolar displacements have a significant effect on the electronic structure of the superlattice. As mentioned earlier, bulk  $\text{LaFeO}_3$  is an insulator with half-filled Fe 3d states, while bulk  $\text{SrFeO}_3$  has hole states near the Fermi energy, due to the d<sup>4</sup> configuration of Fe<sup>4+</sup> (Supporting Figure S7). For the superlattice, holes would then be expected to be present mostly

within the  $\text{La}_{0.5}\text{Sr}_{0.5}\text{FeO}_3$  unit cells. Indeed, we find them to be confined to the Fe 3d–O 2p hybridized states, of the  $\text{La}_{0.5}\text{Sr}_{0.5}\text{FeO}_3$  unit cells, but only when the antipolar distortions of Fe and O ions are forbidden in the simulations. However, with the antipolar distortions, which lower the total energy of the system by  $0.18 \text{ eV/Fe atom}$ , we find that the holes shift to the Fe and O atoms of the  $\text{LaFeO}_3$  unit cells, as shown in Figure 3b. This also leads to segregation of charges on the two different Fe atoms as obtained from the magnetic moments within the PAW spheres.<sup>56</sup> The Fe atoms within the  $\text{La}_{0.5}\text{Sr}_{0.5}\text{FeO}_3$  unit cells have a moment of  $4.1 \mu_B$ , while those within  $\text{LaFeO}_3$  units have a moment of  $3.5 \mu_B$ .<sup>57</sup> Overall, these antipolar distortions and the ensuing changes in electronic properties have important implications on the stability of oxygen vacancies, as we discuss later.

From the previous calculations, it is apparent that neither the experimentally observed polar displacements nor their magnitudes are reproduced. Hence, we systematically introduce different distortions and imperfections in the superlattice to check if we can gain any insights about the experimental polar displacements. As discussed in the Supporting Information, we find that neither octahedral rotations nor different surface terminations reproduce the experimental polar displacements in these epitaxially strained superlattices, which combined with the observed dilation of the LaO-LaO layers (Figure 1c) lead us to investigate the effect of oxygen vacancies. There are four different oxygen sites in the superlattice: in the LaO layer, in the SrO layer, and in the two  $\text{FeO}_2$  layers within the  $\text{LaFeO}_3$  and the  $\text{La}_{0.5}\text{Sr}_{0.5}\text{FeO}_3$  units, respectively. Among these, we find that the oxygen vacancy within the  $\text{FeO}_2$  layer of the  $\text{LaFeO}_3$  unit has the lowest formation energy of  $0.26 \text{ eV}$ , followed by one in the  $\text{FeO}_2$  layer of the  $\text{La}_{0.5}\text{Sr}_{0.5}\text{FeO}_3$  unit, which has a formation energy of  $0.36 \text{ eV}$ . Oxygen vacancies in the LaO layer and the SrO layer have higher formation energies of  $0.41$  and  $0.72 \text{ eV}$ , respectively. The lower formation energy of an oxygen vacancy in the  $\text{LaFeO}_3$  units is in excellent agreement with the experimentally observed dip in the O K EELS intensity within the  $\text{LaFeO}_3$  units, as shown earlier in Figure 2a and b. This preference for the oxygen vacancy comes from the localization of the hole within the  $\text{LaFeO}_3$  units (Figure 3b), which itself is a result of the antipolar distortions within the  $\text{La}_{0.5}\text{Sr}_{0.5}\text{FeO}_3$  units, as mentioned earlier. Forbidding the antipolar distortions, in turn, makes the  $\text{La}_{0.5}\text{Sr}_{0.5}\text{FeO}_3$  units more accommodating to oxygen vacancies by lowering their formation energies (Table S1 in the Supporting Information). We also find that it is energetically favorable to accommodate a higher concentration of oxygen vacancies in the  $\text{FeO}_2$  layer of the  $\text{LaFeO}_3$  units since the cost of removing one-half of the oxygen atoms in that layer is similar ( $0.21 \text{ eV}$  per oxygen vacancy) to that of the creating the initial vacancy.

Oxygen vacancies have major influence on the structure and properties of the superlattice. We find that even a single vacancy in a 120 atom supercell breaks the periodic antipolar displacement pattern of the Fe atoms in the defect free superlattice (Figure 4) giving rise to a net finite polar displacement for the superlattice. We observe that increasing oxygen vacancies leads to larger Fe cation displacements in some layers along with the accompanying chemical expansion (Supporting Figure S10).<sup>10,28,39</sup> This increase in Fe cation displacements can be seen from Figure 4, where the magnitude of some of the displacements reach  $0.1 \text{ \AA}$ . We also find that the oxygen vacancy in the  $\text{LaFeO}_3$  units donates its electrons to the nearby Fe atoms which leads to an increased Fe-moment of  $4.1$

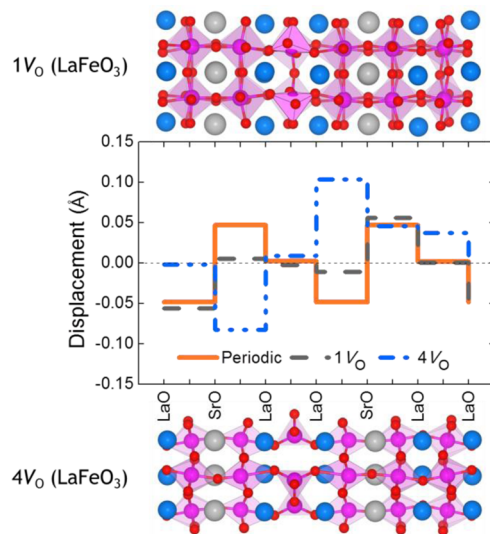


**Figure 4.** Out-of-plane displacement of Fe ions with two different concentrations of oxygen vacancy in a  $\text{FeO}_2$  layer within one  $\text{LaFeO}_3$  unit cell as shown in the structures.

$\mu_{\text{B}}$  compared to their original value of  $3.5 \mu_{\text{B}}$  in the defect free superlattice. Removing half the oxygen atoms from one of the  $\text{LaFeO}_3$  units, in turn, increases the average moment of the Fe atoms in the superlattice to  $4 \mu_{\text{B}}$ . This is also in agreement with the experimentally obtained uniform valence of  $\text{Fe}^{3+}$  as discussed earlier.

Given the inhomogeneous distribution of oxygen vacancies in the films, a perfect match between the experimental observations and the theoretical calculations would require extremely large supercells, which are beyond the scope of current DFT techniques. Nonetheless, our calculated results show that, while commonly studied factors, such as octahedral tilts, strain, and surfaces, fail to explain the experimentally observed polar displacement in the  $(\text{LaFeO}_3)_2/(\text{SrFeO}_3)$  superlattices, oxygen vacancies lead to finite polar displacements. The calculations also explain the presence of oxygen vacancies in the  $\text{LaFeO}_3$  unit cells as observed in the experiments, rather than in the  $\text{La}_{0.5}\text{Sr}_{0.5}\text{FeO}_3$  unit cells, if one were to follow conventional arguments. Together, the experiments and calculations allow us to conclude that the polar behavior in these superlattices is induced by the presence of oxygen vacancies that preferentially accumulate in the  $\text{LaFeO}_3$  unit cells. These results open up a new pathway to design new ferroelectrics and multiferroics. Crucially, an approach like this requires the initial state with a built-in polar asymmetry that can create a preference for oxygen vacancy ordering, which in this case was achieved by using an artificially ordered heterostructure. Further, as has been shown recently, by changing the oxygen partial-pressure, temperature, or through epitaxial strain,<sup>58–60</sup> it could also be possible to control the concentration and ordering of oxygen vacancies in the lattice, thus providing useable instruments of control over the vacancy-induced polar displacements. For instance, it could be possible to switch from a polar state to a nonpolar state by annealing out the oxygen vacancies, which as the calculations show lead to a zero net polar displacement in the superlattice.

**Methods. Film Growth.** The  $(\text{LaFeO}_3)_2/(\text{SrFeO}_3)$  superlattice was grown by ozone-assisted molecular beam epitaxy on a (001)  $\text{SrTiO}_3$  substrate at  $650^\circ\text{C}$ . The  $\text{SrTiO}_3$  substrate was etched in BHF solution and followed by annealing at  $1050^\circ\text{C}$

for 2 h prior to growth to ensure well-formed terraces with  $\text{TiO}_2$  termination. During the growth, the ozone pressure in the chamber was fixed at  $2 \times 10^{-6}$  Torr. For the growth of  $(\text{LaFeO}_3)_2/(\text{SrFeO}_3)$  superlattice, the following layer sequence was used, creating a digital superlattice with a three  $\text{ABO}_3$  units:  $[(\text{LaO}/\text{FeO}_2)(\text{SrO}/\text{FeO}_2)(\text{LaO})(\text{FeO}_2)]$ . The superlattice film was 33 unit cells thick. The growth was monitored by in situ reflection high-energy electron diffraction, and the oscillations in the intensity of specular spots were observed during the growth of each layer.

**STEM Imaging and EELS Analysis.** A 100 kV aberration-corrected scanning transmission electron microscope (NION UltraSTEM) equipped with a cold field emission electron gun and a corrector of third and fifth order aberrations was used for ADF STEM imaging for the sample. The convergence semiangle of the incident electron probe was 30 mrad and the detector inner angle of ADF imaging,  $\sim 86$  mrad. The cross-sectional sample studied for STEM was prepared by conventional mechanical thinning, polishing, and ion-milling process.

EELS data were acquired using a Gatan Enfina spectrometer attached to the microscope. The EELS collection semiangle was 48 mrad, and the EELS SI data for the superlattice film were recorded from 490 to 892 eV with 0.3 eV/ch and 0.2 s/pixel dwell time on a  $25 \times 63$  spatial pixel grids. The film thickness in the observed sample was measured to be ranging from 40 to 45 nm by EELS log-ratio method. Noise in the acquired ADF STEM images was removed by using a maximum entropy method<sup>61</sup> (DECONVHAADF software package commercialized by HREM Research Inc.). ADF STEM image simulation to compare with the experimental data was carried out using the QSTEM software package.<sup>62</sup>

**Calculation Details.** DFT calculations were performed using a plane-wave basis set with a cutoff energy of 525 eV and the projector-augmented-wave method (PAW)<sup>56</sup> as implemented within the Vienna ab initio simulation package (VASP) code.<sup>63,64</sup> Electron exchange and correlation effects were described within the generalized gradient approximation (GGA).<sup>65</sup> We used a large ( $2 \times 2 \times 6$ ) superlattice of the 5-atom perovskite unit cells for the calculations. The large supercell was used in order to reduce the effect of image interactions for the calculations with oxygen vacancies. To simulate the epitaxial growth on  $\text{SrTiO}_3$ , the in-plane lattice constants were constrained to match the theoretical  $\text{SrTiO}_3$  lattice constant of 3.945 Å, and the cell volume was relaxed along the z-direction (i.e., [001] growth direction). The ions were allowed to relax until forces per ion were smaller than 5 meV/Å. The Brillouin zone was sampled using a  $2 \times 2 \times 1$  Monkhorst-Pack  $k$ -points mesh<sup>66</sup> for relaxations and a denser  $4 \times 4 \times 1$   $\Gamma$ -centered mesh for electronic calculations. Further, transition-metal atoms, such as Fe, have localized d-electrons giving rise to strong correlations, which are usually not correctly described by GGA. To address this issue, we have included the effect of strong correlations by using the DFT+U approach.<sup>67</sup> Specifically, we used the rotationally invariant Dudarev approach<sup>68</sup> to DFT+U, in which only one effective Hubbard parameter  $U_{\text{eff}} = U - J$  is used, with  $U$  and  $J$  being Hubbard repulsion and intra-atomic exchange, respectively, for the electrons in the localized d-states. We used  $U_{\text{eff}}$  of 5.1 eV for Fe for the electronic calculations, based on the recent work by Hong et al.<sup>69</sup> The formation energies of oxygen vacancies have also been calculated using GGA+U, as the GGA energies have been shown to be significantly higher than the experimental formation energies in bulk  $\text{La}_x\text{Sr}_{1-x}\text{O}_{3-\delta}$  systems.<sup>30</sup>

## ■ ASSOCIATED CONTENT

### ● Supporting Information

Additional experimental and calculation details, figures, and tables. This material is available free of charge via the Internet at <http://pubs.acs.org>.

## ■ AUTHOR INFORMATION

### Corresponding Authors

\*(R.M.) E-mail: rohan.mishra@vanderbilt.edu.

\*(A.Y.B.) E-mail: albinab@ornl.gov.

### Author Contributions

▽ These authors contributed equally.

### Notes

The authors declare no competing financial interest.

## ■ ACKNOWLEDGMENTS

This research was supported by the Materials Sciences and Engineering Division, Office of Basic Energy Sciences (BES), U.S. Department of Energy (DOE) (R.M., Y.M.K., A.B., D.D.F., S.J.P., S.T.P., A.Y.B.) and through a user project supported by Oak Ridge National Laboratory's Center for Nanophase Materials Sciences, which is sponsored by the Scientific User Facilities Division, Office of BES, U.S. DOE, and DOE grant DE-FG02-09ER46554 (S.T.P.). J.S. was supported by the ERC grant #239739 STEMOX and Juan de la Cierva program JCI-2011-09428 (MICINN-Spain). Work at Argonne National Laboratory, including use of facilities at the Center for Nanoscale Materials, was supported by the DOE, BES, under contract no. DE-AC02-06CH11357. This research used resources of the National Energy Research Scientific Computing Center, which is supported by the Office of Science of the U.S. DOE under contract no. DE-AC02-05CH11231.

## ■ REFERENCES

- (1) Hill, N. A. *J. Phys. Chem. B* **2000**, *104*, 6694–6709.
- (2) Cohen, R. E. *Nature* **1992**, *358*, 136–138.
- (3) Wang, J.; et al. *Science* **2003**, *299*, 1719–22.
- (4) Fennie, C. J.; Rabe, K. M. *Phys. Rev. Lett.* **2006**, *97*, 267602.
- (5) Lee, J. H.; et al. *Nature* **2010**, *466*, 954–958.
- (6) Van Aken, B. B.; Palstra, T. T. M.; Filippetti, A.; Spaldin, N. A. *Nat. Mater.* **2004**, *3*, 164–170.
- (7) Fennie, C. J.; Rabe, K. M. *Phys. Rev. B* **2005**, *72*, 100103.
- (8) Ikeda, N.; et al. *Nature* **2005**, *436*, 1136–1138.
- (9) Kimura, T.; Goto, T.; Shintani, H.; Ishizaka, K.; Arima, T.; Tokura, Y. *Nature* **2003**, *426*, 55–58.
- (10) Kim, Y.-M.; et al. *Nat. Mater.* **2012**, *11*, 888–894.
- (11) Kalinin, S. V.; Borisevich, A. Y.; Fong, D. D. *ACS Nano* **2012**, *6*, 10423–10437.
- (12) Dagotto, E. *Science* **2005**, *309*, 257–262.
- (13) Tokura, Y.; Nagaosa, N. *Science* **2000**, *288*, 462–468.
- (14) Cortés-Gil, R.; Ruiz-González, L.; Alonso, J. M.; García-Hernández, M.; Hernando, A.; González-Calbet, J. M. *Chem. Mater.* **2012**, *24*, 2519–2526.
- (15) Gazquez, J.; et al. *Nano Lett.* **2011**, *11*, 973–976.
- (16) Biškup, N.; Salafranca, J.; Mehta, V.; Oxley, M. P.; Suzuki, Y.; Pennycook, S. J.; Pantelides, S. T.; Varela, M. *Phys. Rev. Lett.* **2014**, *112*, 087202.
- (17) Kalinin, S. V.; Spaldin, N. A. *Science* **2013**, *341*, 858–859.
- (18) Wang, R.; et al. *Phys. Rev. Lett.* **2009**, *102*, 047601.
- (19) Chisholm, M. F.; Luo, W.; Oxley, M. P.; Pantelides, S. T.; Lee, H. N. *Phys. Rev. Lett.* **2010**, *105*, 197602.
- (20) Kim, Y.-M.; Oxley, M. P.; Morozovska, A.; Eliseev, E.; Yu, P.; Chu, Y.-H.; Ramesh, R.; Pennycook, S.; Kalinin, S.; Borisevich, A. Abstracts of Papers, APS March Meeting, Baltimore, MD, Mar 18–22, 2013. <http://meetings.aps.org/link/BAPS.2013.MAR.C14.10>.
- (21) Glazer, A. M. *Acta Crystallogr., Sect. B: Struct. Sci.* **1972**, *28*, 3384–3392.
- (22) Woodward, P. M. *Acta Crystallogr., Sect. B: Struct. Sci.* **1997**, *53*, 32–43.
- (23) Koehler, W.; Wollan, E. *J. Phys. Chem. Solids* **1957**, *2*, 100–106.
- (24) Takeda, T.; Yamaguchi, Y.; Watanabe, H. *J. Phys. Soc. Jpn.* **1972**, *33*, 967–969.
- (25) Mizusaki, J.; Sasamoto, T.; Cannon, W. R.; Bowen, H. K. *J. Am. Ceram. Soc.* **1983**, *66*, 247–252.
- (26) Cheng, J.; Navrotsky, A.; Zhou, X.; Anderson, H. U. *Chem. Mater.* **2005**, *17*, 2197–2207.
- (27) Dann, S. E.; Currie, D. B.; Weller, M. T.; Thomas, M. F.; Al-Rawwas, A. D. *J. Solid State Chem.* **1994**, *109*, 134–144.
- (28) Chen, X.; Grande, T. *Chem. Mater.* **2013**, *25*, 3296–3306.
- (29) Fossdal, A.; Menon, M.; Waernhus, I.; Wiik, K.; Einarsrud, M.-A.; Grande, T. *J. Am. Ceram. Soc.* **2004**, *87*, 1952–1958.
- (30) Ritzmann, A. M.; Muñoz-García, A. B.; Pavone, M.; Keith, J. A.; Carter, E. A. *Chem. Mater.* **2013**, *25*, 3011–3019.
- (31) Battle, P. D.; Gibb, T. C.; Lightfoot, P. J. *Solid State Chem.* **1990**, *84*, 271–279.
- (32) Battle, P. D.; Gibb, T. C.; Lightfoot, P. J. *Solid State Chem.* **1990**, *84*, 237–244.
- (33) *Scanning Transmission Electron Microscopy: Imaging and Analysis*; Pennycook, S. J., Nellist, P. D., Eds.; Springer: New York, 2011.
- (34) Borisevich, A. Y.; et al. *Phys. Rev. Lett.* **2010**, *105*, 087204.
- (35) Chang, H. J.; et al. *Adv. Mater.* **2011**, *23*, 2474–2479.
- (36) Kim, Y.-M.; et al. *Adv. Mater.* **2013**, *25*, 2497–2504.
- (37) Shannon, R. D. *Acta Crystallogr., Sect. A* **1976**, *32*, 751–767.
- (38) Adler, S. B. *J. Am. Ceram. Soc.* **2001**, *84*, 2117–2119.
- (39) Marrocchelli, D.; Bishop, S. R.; Tuller, H. L.; Watson, G. W.; Yildiz, B. *Phys. Chem. Chem. Phys.* **2012**, *14*, 12070–12074.
- (40) For a discussion regarding the observed oxygen vacancy profile, please see the Supporting Information.
- (41) Jang, J. H.; Mishra, R.; Kim, Y.-M.; He, Q.; Qiao, L.; Biegalski, M. D.; Lupini, A. R.; Pantelides, S. T.; Pennycook, S. J.; Kalinin, S. V.; Borisevich, A. Y. Abstracts of Papers, APS March Meeting, Denver, CO, Mar 3–7, 2014. <http://meetings.aps.org/link/BAPS.2014.MAR.S49.12>.
- (42) Kretschmer, R.; Binder, K. *Phys. Rev. B* **1979**, *20*, 1065–1076.
- (43) Jia, C.-L.; Nagarajan, V.; He, J.-Q.; Houben, L.; Zhao, T.; Ramesh, R.; Urban, K.; Waser, R. *Nat. Mater.* **2007**, *6*, 64–69.
- (44) Willmott, P.; et al. *Phys. Rev. Lett.* **2007**, *99*, 155502.
- (45) Gerra, G.; Tagantsev, A. K.; Setter, N.; Parlinski, K. *Phys. Rev. Lett.* **2006**, *96*, 107603.
- (46) Canton, C.; et al. *Adv. Mater.* **2012**, *24*, 3952–3957.
- (47) Stengel, M. *Phys. Rev. Lett.* **2011**, *106*, 136803.
- (48) Botton, G. A.; Appel, C. C.; Horsewell, A.; Stobbs, W. M. *J. Microsc.* **1995**, *180*, 211–216.
- (49) Schmid, H. K.; Mader, W. *Micron* **2006**, *37*, 426–432.
- (50) Cavé, L.; Al, T.; Loomer, D.; Cogswell, S.; Weaver, L. *Micron* **2006**, *37*, 301–309.
- (51) We have calculated the stability of different magnetic ordering of the Fe spins and find the G-type antiferromagnetic ordering to be energetically most stable.
- (52) King, G.; Woodward, P. M. *J. Mater. Chem.* **2010**, *20*, 5785.
- (53) Nakajima, T.; Kageyama, H.; Yoshizawa, H.; Ueda, Y. *J. Phys. Soc. Jpn.* **2002**, *71*, 2843–2846.
- (54) Pruneda, J. M.; Ferrari, V.; Rurrali, R.; Littlewood, P. B.; Spaldin, N. A.; Artacho, E. *Phys. Rev. Lett.* **2007**, *99*, 226101.
- (55) Chen, H.; Ismail-Beigi, S. *Phys. Rev. B* **2012**, *86*, 024433.
- (56) Blöchl, P. E. *Phys. Rev. B* **1994**, *50*, 17953–17979.
- (57) The moments have been obtained using a  $U_{\text{eff}} = 5.1$  eV on Fe. In order to relate the magnetic moments with nominal oxidation states, we use the following relation.  $\text{Fe}^{3+}$  ( $d^5$ ) in high-spin state would correspond to a magnetic moment of  $5\mu_B$ , while  $\text{Fe}^{4+}$  ( $d^4$ ) would correspond to a lower moment of  $4\mu_B$ .
- (58) Aschner, U.; Pfenniger, R.; Selbach, S. M.; Grande, T.; Spaldin, N. A. *Phys. Rev. B* **2013**, *88*, 054111.

- (59) Gazquez, J.; Bose, S.; Sharma, M.; Torija, M. A.; Pennycook, S. J.; Leighton, C.; Varela, M. *APL Mater.* **2013**, *1*, 012105.
- (60) Jeen, H.; et al. *Nat. Mater.* **2013**, *12*, 1057–1063.
- (61) Gull, S. F.; Skilling, J. Communications, Radar and Signal Processing. *IEE Proc. F* **1984**, *131*, 646–659.
- (62) Koch, C. T. Determination of core structure periodicity and point defect density along dislocations. Ph.D. thesis, Arizona State University, Phoenix, AZ, 2002.
- (63) Kresse, G.; Hafner, J. *Phys. Rev. B* **1993**, *47*, 558–561.
- (64) Kresse, G.; Hafner, J. *Phys. Rev. B* **1994**, *49*, 14251–14269.
- (65) Wang, Y.; Perdew, J. *Phys. Rev. B* **1991**, *44*, 13298–13307.
- (66) Monkhorst, H. J.; Pack, J. D. *Phys. Rev. B* **1976**, *13*, 5188–5192.
- (67) Anisimov, V.; Zaanen, J.; Andersen, O. *Phys. Rev. B* **1991**, *44*, 943–954.
- (68) Dudarev, S.; Botton, G.; Savrasov, S.; Humphreys, C.; Sutton, A. *Phys. Rev. B* **1998**, *57*, 1505–1509.
- (69) Hong, J.; Stroppa, A.; Íñiguez, J.; Picozzi, S.; Vanderbilt, D. *Phys. Rev. B* **2012**, *85*, 054417.